LRRTM3 regulates activity-dependent synchronization of synapse properties in topographically connected hippocampal neural circuits

Jinhu Kim[a,1], Dongseok Park[a,1], Na-Young Seo[a,b,1], Taek-Han Yoon[a,1], Gyu Hyun Kim[b], Sang-Hoon Lee[b,c], Jinsoo Seo[a], Ji Won Um[a], Kea Joo Lee[a,b,2], and Jaewon Ko[a,2]

[a]Department of Brain and Cognitive Sciences, Daegu Gyeongbuk Institute of Science and Technology (DGIST), Daegu 42988, Korea; [b]Neural Circuits Group, Korea Brain Research Institute (KBRI), Daegu 41062, Korea; and [c]Brain Research Core Facilities, KBRI, Daegu 41062, Korea

Edited by Robert Malenka, Stanford University, Stanford, CA; received June 5, 2021; accepted December 3, 2021

Synaptic cell-adhesion molecules (CAMs) organize the architecture and properties of neural circuits. However, whether synaptic CAMs are involved in activity-dependent remodeling of specific neural circuits is incompletely understood. Leucine-rich repeat transmembrane protein 3 (LRRTM3) is required for the excitatory synapse development of hippocampal dentate gyrus (DG) granule neurons. Here, we report that *Lrrtm3*-deficient mice exhibit selective reductions in excitatory synapse density and synaptic strength in projections involving the medial entorhinal cortex (MEC) and DG granule neurons, accompanied by increased neurotransmitter release and decreased excitability of granule neurons. LRRTM3 deletion significantly reduced excitatory synaptic innervation of hippocampal mossy fibers (Mf) of DG granule neurons onto thorny excrescences in hippocampal CA3 neurons. Moreover, LRRTM3 loss in DG neurons significantly decreased mossy fiber long-term potentiation (Mf-LTP). Remarkably, silencing MEC–DG circuits protected against the decrease in the excitatory synaptic inputs onto DG and CA3 neurons, excitability of DG granule neurons, and Mf-LTP in *Lrrtm3*-deficient mice. These results suggest that LRRTM3 may be a critical factor in activity-dependent synchronization of the topography of MEC–DG–CA3 excitatory synaptic connections. Collectively, our data propose that LRRTM3 shapes the target-specific structural and functional properties of specific hippocampal circuits.

dentate gyrus | excitatory synapse | long-term plasticity | LRRTM3 | medial entorhinal cortex

Synapses are critical determinants of the properties of neural circuits during nervous system development, likely through multiple *trans*-synaptic recognition processes (1–3). Several candidate synaptic cell-adhesion molecules (CAMs) that physically bridge the synaptic cleft and functionally align pre- and postsynaptic neurons have been identified (4). For example, neurexins (Nrxns) and neuroligins (Nlgns) have been found responsible across diverse brain areas for specific synaptic properties (reviewed in ref. 5). In addition to Nrxns and Nlgns, other cell-surface proteins have been described to regulate topographic wiring and assembly of specific neural circuits, including latrophilin-2 for layer III entorhinal cortex (EC)–hippocampal CA1 and teneurin-3 for proximal CA1–distal subiculum (6, 7). Although these proteins determine synaptic specificity, consistent with their distribution at specific synapses, the prediction of the putative function of specific synaptic CAMs at specific neural circuits is not always straightforward (8–10).

LRRTMs (leucine-rich repeat transmembrane proteins) are a family of synaptic CAMs expressed only in vertebrate brains (11, 12). All four LRRTM family members regulate the structure, transmission, and plasticity of excitatory synapses in the hippocampus (13–17), likely by binding to presynaptic Nrxns and PSD-95 PDZ proteins (13, 18–20). Intriguingly, LRRTM1 and LRRTM2, together with Nlgn1 and Nlgn3, cooperate to maintain normal levels of excitatory synapses in an activity-dependent manner (14). In contrast to several previous studies (21, 22), X-ray crystallographic analysis suggested that, in contrast to LRRTM1 and LRRTM2, LRRTM3 and LRRTM4 do not bind to Nrxns (23). However, a recent study showed that LRRTM3 and LRRTM4 employ heparan sulfate moieties for binding to Nrxns and further form complexes with PTPσ to organize excitatory synapse development (24, 25).

Each *Lrrtm* gene exhibits distinct expression patterns, at least at the messenger RNA (mRNA) level, consistent with their putative synaptic roles. We previously showed that LRRTM3 regulates the excitatory structure and transmission of postsynaptic dentate gyrus (DG) granule neurons, with LRRTM3 deletion resulting in increased neurotransmitter release (26). Moreover, LRRTM4, another LRRTM family protein with a hippocampal distribution pattern similar to that of LRRTM3, was recently reported to be expressed at GABAergic synapses of axon terminals in rod bipolar cells, where it mediates presynaptic inhibition and assembly

Significance

The present study utilized imaging, electrophysiology, and three-dimensional high-resolution electron microscopy analyses to address the neural circuit role of LRRTM3 in vivo, using both conventional and conditional *Lrrtm3*-KO mice. We found that LRRTM3 is required for the specific assembly and function of the medial perforant path to dentate gyrus synapses. Moreover, LRRTM3 is required for proper excitatory synaptic connectivity and long-term synaptic plasticity at mossy fiber–CA3 synapses. Strikingly, presynaptic inactivation of medial perforant path–dentate gyrus (MPP–DG) circuit activities completely rescued the impaired excitatory synaptic inputs and long-term synaptic plasticity of *Lrrtm3*-KO mice, demonstrating that LRRTM3 is involved in activity-dependent hippocampal excitatory synapse refinement/stabilization, which is dictated and synchronized by glutamatergic neurotransmission.

Author contributions: K.J.L. and J. Ko designed research; J. Kim, D.P., N.-Y.S., T.-H.Y., and G.H.K. performed research; J.S. and J.W.U. contributed new reagents/analytic tools; J. Kim, D.P., N.-Y.S., T.-H.Y., G.H.K., S.-H.L., J.S., J.W.U., K.J.L., and J. Ko analyzed data; and K.J.L. and J. Ko wrote the paper.

The authors declare no competing interest.

This article is a PNAS Direct Submission.

[1]J. Kim, D.P., N.-Y.S., and T.-H.Y. contributed equally to this work.

[2]To whom correspondence may be addressed. Email: relaylee@kbri.re.kr or jaewonko@dgist.ac.kr.

This article contains supporting information online at http://www.pnas.org/lookup/suppl/doi:10.1073/pnas.2110196119/-/DCSupplemental.

Published January 12, 2022.

(27). These results suggest that a subset of LRRTMs is expressed in presynaptic neurons of certain brain areas.

DG mossy fiber (Mf)–CA3 synapses in the hippocampus have been extensively used as a model to investigate mechanisms of activity-dependent homeostatic synaptic plasticity and target-specific synaptic specificity (28, 29). Highly plastic presynaptic Mf terminals with massive separate vesicle release sites of glutamatergic DG neurons connect to multiheaded postsynaptic spines of CA3 (called thorny excrescences [TEs]), and filopodia projecting from the Mf boutons (MfBs) connect with nearby GABAergic interneurons to provide feed-forward inhibition of CA3 neurons during a subset of cognitive tasks (30). In addition, the Mf–CA3 synapses exhibit structural plasticity at both presynaptic Mf terminals and postsynaptic TEs that are sensitive to changes in levels of activity within the hippocampus (31). Moreover, these structural alterations are involved in encoding CA3-dependent contextual memory formation. Several classes of synaptic proteins, including the cell-surface proteins SynCAM1 and Kirrel3 and the transcription factor Npas4, act as target-specific cues, likely balancing network excitability and permitting homeostatic adjustment (32–34). Knockout (KO) mice deficient for SynCAM1 or Npas4 showed impaired contextual memory formation or impaired spatial memory, suggesting that these factors may regulate learning-induced synaptic plasticity at Mf–CA3 synapses during cognitive tasks.

In the present study, we show that LRRTM3 is specifically required for the maintenance of excitatory synaptic structures and strength within medial EC (MEC), but not lateral EC (LEC), projections. Unexpectedly, the loss of LRRTM3 decreased the density of MfBs and TEs. Moreover, LRRTM3 deletion in DG granule neurons reduced excitatory synaptic innervations in a subset of hippocampal CA3 layers and altered axonal projections onto the hippocampal CA3 neurons. These morphological phenotypes in *Lrrtm3*-deficient mice were accompanied by reduced long-term potentiation (LTP) at Mf–CA3 synapses. Furthermore, presynaptic silencing of MEC projections in DG-specific LRRTM3-KO mice normalized the impaired excitatory synapse development of DG and CA3 regions and rescued Mf-LTP. Collectively, our findings identify LRRTM3 as a regulator of specific hippocampal circuit connectivity and plasticity, which can be remodeled in an activity-dependent manner.

Results

LRRTM3 Is Primarily Expressed in Granule Neurons in the Hippocampal Dentate Gyrus. Previous in situ hybridization (ISH) analyses using isotope-labeled gene-specific probes showed that both LRRTM3 splice variants are strongly expressed in the hippocampal DG, but not in other hippocampal subfields (26, 35). However, it was unknown whether LRRTM3 transcripts are specifically expressed in granule neurons and/or other types of neurons (i.e., interneurons or mossy cells in the hilus). RNAscope-based ISH analyses were thus performed to assess the expression of *Lrrtm3* mRNAs in the hippocampal DG region. *Lrrtm3* mRNAs are mainly expressed in granule neurons, but they are also expressed in *Gad1*$^+$ GABAergic interneurons and/or *Calb2*$^+$ mossy cells in the hilus (*SI Appendix*, Fig. S1). Parallel RNAscope ISH analyses using probes specific for each *Lrrtm* indicated that all four *Lrrtm* mRNAs are expressed in *Prox1*$^+$ granule neurons (*SI Appendix*, Fig. S1 *A–C*). Notably, *Lrrtm1*, *Lrrtm2*, and *Lrrtm4* mRNAs are comparably expressed in *Gad1*$^+$ GABAergic interneurons, whereas *Lrrtm3* mRNAs are primarily expressed in *Prox1*$^+$ granule neurons (*SI Appendix*, Fig. S1 *B–E*). Immunoblotting using antibodies specific to the long form of LRRTM3 (L3L) showed that this splice variant is expressed in the presynaptic vesicle fraction (26). Because these in-house L3L-specific antibodies were not suitable for immunohistochemistry, we could not determine whether L3L is expressed in Mf axons and/or filopodia that connect DG axons to dendrites of GABAergic interneurons. Our RNAscope-based ISH analyses further confirmed that *Lrrtm3* mRNAs are not prominently expressed in other hippocampal areas (26, 35) (*SI Appendix*, Fig. S1*A*).

LRRTM3 Loss Decreases Excitatory Synaptic Inputs Specifically from the Medial Entorhinal Cortex to the Dentate Gyrus. LRRTM3 was previously shown to be responsible for excitatory synapse development in hippocampal DG granule neurons, similar to other LRRTMs (13–17, 19–21, 26, 36). However, it remained unclear whether LRRTM3 is required for biasing entorhinal cortical projections that innervate specific dendritic compartments of DG granule neurons in vivo. Serial-section electron microscopy using LRRTM3 knockout (*Lrrtm3*-KO) mice revealed that the numbers of synapses formed on dendritic spines were significantly decreased in the middle (MML), but not the outer (OML), molecular layer in *Lrrtm3*-KO mice (Fig. 1 *A–C*), in line with our previous findings (26). The shaft synapse density of wild-type (WT) and *Lrrtm3*-KO mice, however, did not differ. In addition, *Lrrtm3*-KO mice had a significantly smaller postsynaptic density (PSD) in the MML, but not the OML, than did WT mice (Fig. 1 *A*, *D*, and *E*), suggesting that LRRTM3 might have a layer- or input-specific role in excitatory synapse formation in the DG.

To further probe whether LRRTM3 deletion can functionally impact a specific perforant pathway (PP), we generated *Lrrtm3* conditional KO (cKO) mice in which exons 1 and 2 were flanked by loxP sites (*Lrrtm3*$^{f/f}$) to allow Cre recombinase–dependent LRRTM3 deletion (*SI Appendix*, Fig. S2 *A* and *B*). We then stereotactically injected adeno-associated viruses (AAVs) expressing either inactive (ΔCre) or active Cre recombinase into the hippocampal DG region of *Lrrtm3*$^{f/f}$ mice. LRRTM3 deletion in vivo was validated by qRT-PCR analyses (*SI Appendix*, Fig. S2*C*) and semiquantitative immunoblot analyses using hippocampal DG tissue lysates of AAV-injected mice (*SI Appendix*, Fig. S2 *D* and *E*).

LRRTM3 Loss Impairs Excitatory Synaptic Strength from the Medial Entorhinal Cortex to the Dentate Gyrus. To corroborate our anatomical results, we performed electrophysiological recording of DG granule neurons from both WT and *Lrrtm3*-cKO mice (Fig. 1 *F–S* and *SI Appendix*, Fig. S3). Notably, the frequency, but not the amplitude, of spontaneous excitatory postsynaptic currents (sEPSCs) was massively reduced in *Lrrtm3*-cKO mice (*SI Appendix*, Fig. S3 *B–D*). Moreover, the frequency, but not the amplitude, of miniature excitatory postsynaptic currents (mEPSCs) was also reduced in *Lrrtm3*-cKO mice (*SI Appendix*, Fig. S3 *E–G*). Furthermore, current-clamp recordings revealed that action potential firing rate of DG granule neurons induced by current injections was significantly lower in *Lrrtm3*-cKO slices than in control slices (*SI Appendix*, Fig. S3 *H* and *I*). In addition, we induced LTP of medial perforant path (MPP) to DG granule neurons through high-frequency stimulation to determine whether there are any alterations in MPP–DG LTP in *Lrrtm3*-cKO mice. These experiments revealed a significant reduction in PP–DG LTP (~34%) in *Lrrtm3*-cKO mice (*SI Appendix*, Fig. S3 *J–M*). These results reaffirm that conditional LRRTM3 deletion impairs excitatory synaptic transmission and the excitability of DG granule neurons, in addition to a reduction in MPP–DG LTP.

We next asked whether postsynaptic deletion of LRRTM3 could impair the excitatory synaptic strength at specific PPs, as predicted by the decreased synapse number seen in the MML region of *Lrrtm3*-KO mice (Fig. 1 *A*, *B*, and *D*). To this end, we electrically stimulated the axonal fibers of the MPP or lateral PP (LPP), which target the medial or outer molecular layers of

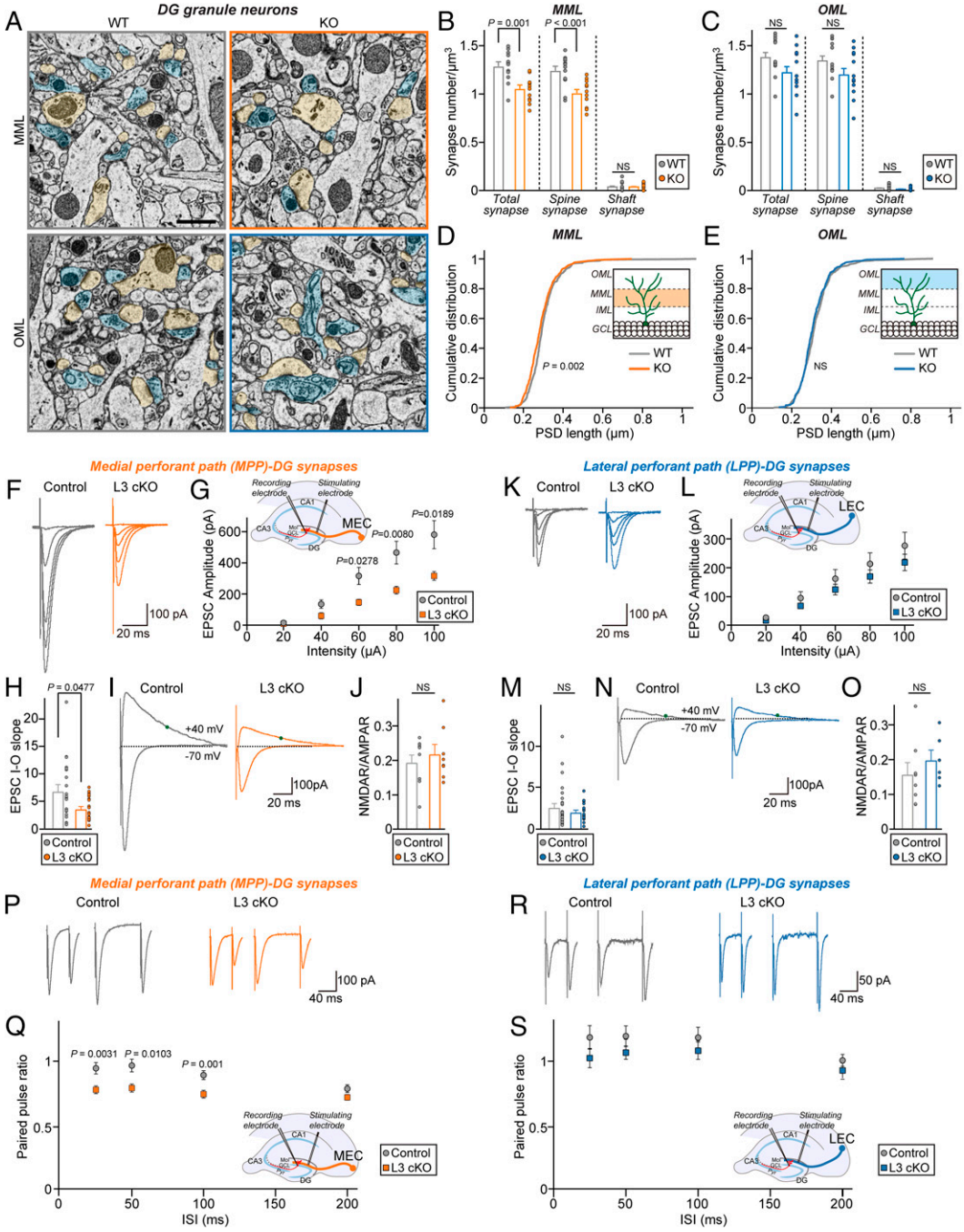

Fig. 1. Reduced excitatory synaptic density and strength at MPP–DG synapses of LRRTM3-deficient mice. (*A*) Representative EM images of synapses on dendritic shafts or spines in the MML and OML of the DG in WT and *Lrrtm3*-KO mice. Areas marked in light sky blue and yellow indicate presynaptic and postsynaptic sites, respectively (Scale bar, 1 μm). (*B* and *C*) Mean number of synapses per unit volume of MML (*B*) and OML (*C*) in WT (gray bar) and *Lrrtm3*-KO (orange or blue bar) mice. Data represent means ± SEMs (n = 12 dissector volumes from two mice per genotype per layer; Student's t test). (*D* and *E*) Cumulative distribution plots for the longest PSD lengths of individual spines in the MML (*D*) and OML (*E*) in WT (gray line) and *Lrrtm3*-KO (orange or blue line) mice. Data represent means ± SEMs (WT [MML], n = 485; KO [MML], n = 385 spines; WT [OML], n = 527; KO [OML], n = 466 spines; Kolmogorov–Smirnov test). (*F–H*) Measurements of excitatory synaptic strength via I-O curves of control and L3 cKO mice, showing representative AMPAR-EPSC traces (*F*), summary plotting of the EPSC amplitudes as a function of MPP stimulation current (*G*), and summary graphs of fitted linear I-O slopes (*H*). Data represent means ± SEMs (n denotes the number of recorded neurons; control, n = 21; L3 cKO, n = 23; Mann–Whitney U test). (*I* and *J*) Measurements of NMDAR/AMPAR-EPSC ratios at MPP–DG synapses of control and L3 cKO mice. AMPAR-EPSCs were recorded at −70 mV in the presence of picrotoxins, and NMDAR-EPSCs were then recorded at +40 mV (*I*, representative traces; *J*, summary graphs). (*K–M*) Same as *F–H*, except that AMPAR-EPSCs were recorded in the same neurons as in *F–H* as a function of LPP stimulation. Data represent means ± SEMs (n denotes the number of recorded neurons; control, n = 19; L3 cKO, n = 13; Mann–Whitney U test). (*N* and *O*) Same as *I* and *J*, except that NMDAR/AMPAR-EPSC ratios were measured in the same neurons as in *I* and *J* as a function of LPP stimulation. Data represent means ± SEMs (n denotes the number of recorded neurons; control, n = 8; L3 cKO, n = 6; Mann–Whitney U test). (*P* and *R*) Representative traces of PPRs of EPSCs at MPP–DG synapses (*P*) or LPP–DG synapses (*R*) at two different interstimulus intervals (50 and 100 ms). (*Q* and *S*) EPSC-PPRs at MPP–DG synapses (*Q*) and LPP–DG synapses (*S*) as a function of the indicated interstimulus intervals (50, 100, 150, and 200 ms). Data represent means ± SEMs (n denotes the number of recorded neurons; control [MPP], n = 12; L3 cKO [MPP], n = 14; control [LPP], n = 11; L3 cKO [LPP], n = 10; Mann–Whitney U test). NS, not significant.

the DG, respectively (37–39), and then recorded the evoked excitatory postsynaptic currents (eEPSCs) of DG granule neurons using input–output (I–O) curves to control for the variability in stimulus strength (Fig. 1 *F–H* and *K–M*). The postsynaptic deletion of LRRTM3 decreased MPP-EPSCs by ∼52.6%, but had no significant effect on LPP-EPSCs (Fig. 1 *F–H* and *K–M*). In these measurements, the EPSCs almost exclusively reflected α-amino-3-hydroxy-5-methylisoxazole-4-propionic acid receptor (AMPAR)–mediated responses. However, parallel experiments assessing *N*-methyl-D-aspartate receptor (NMDAR)–mediated responses also showed a decrease in synaptic strength, such that the NMDAR/AMPAR ratio was comparable between control and *Lrrtm3*-cKO neurons (Fig. 1 *I*, *J*, *N*, and *O*). Moreover, the reduced excitatory synaptic strength in the MPP was strikingly accompanied by an increase in the release probability, as reflected by a decreased paired-pulse ratio (PPR) under *Lrrtm3* deletion (Fig. 1 *P* and *Q*). There were no changes in PPRs of the LPP–DG pathway in LRRTM3-deficient neurons (Fig. 1 *R* and *S*). Therefore, our results suggest that LRRTM3 is specifically required to maintain excitatory synaptic strength within MPP–DG projections and might be involved in the up-regulation of presynaptic function.

LRRTM3 Loss Reduces Excitatory Synapse Maintenance at Mossy Fiber–CA3 Excitatory Synapses. We previously reported that the excitatory synaptic transmission and excitability of DG granule neurons were reduced in constitutive *Lrrtm3*-KO mice (26). To confirm that conditional LRRTM3 deletion in DG neurons recapitulates the similar histological phenotypes of constitutive *Lrrtm3*-KO mice, we stereotactically injected AAVs expressing ΔCre or Cre into the hippocampal DG region of *Lrrtm3*$^{f/f}$ mice (*SI Appendix*, Fig. S4 *A* and *B*), and analyzed the density of excitatory and inhibitory synaptic puncta, which were labeled with antibodies to vesicular glutamate transporter 1 (VGLUT1) and vesicular GABA transporter (VGAT), respectively, in sections from the hippocampal DG and CA3 (*SI Appendix*, Fig. S4 *C–F*). Immunohistochemical analyses revealed that the VGLUT1 puncta density was decreased in the DG molecular layers and the hilus (*SI Appendix*, Fig. S4 *C* and *D*). Strikingly, the conditional loss of LRRTM3 from the DG area also reduced the density and area of VGLUT1 puncta in the hippocampal CA3 *stratum oriens* (SO) and *stratum radiatum* (SR) layers (*SI Appendix*, Fig. S4 *C* and *D*), findings similar to those in conventional *Lrrtm3*-KO mice (*SI Appendix*, Fig. S5). The density and area of VGAT puncta were comparable in control and *Lrrtm3*-cKO mice (*SI Appendix*, Fig. S4 *E* and *F*). Taken together, these results show that postsynaptic LRRTM3 is required for innervation of excitatory synaptic inputs at MPP–DG synapses and for excitatory synapse maintenance in a subset of hippocampal CA3 layers.

To assess whether altered synapse properties in DG granule neurons influence the structural connectivity with output neurons, we next performed quantitative immunofluorescence analyses using VGLUT1 or the MfB marker, synaptoporin (SPO), in control and *Lrrtm3*-cKO mice (*SI Appendix*, Fig. S6). The density and area of VGLUT1 puncta were significantly reduced in the SR and SO layers, but not the *stratum lucidum* (SL) layer, of the hippocampal CA3 area (*SI Appendix*, Fig. S4). Mf axons are composed of two distinct bundles targeting CA3 pyramidal neurons: large suprapyramidal bundles (SPBs) traveling adjacent to and above the pyramidal layer and small infrapyramidal bundles (IPBs) traveling below the pyramidal layer, both of which target CA3 pyramidal neurons (40). Thus, we separately quantified the density and area of SPO puncta in each bundle of Mf axons in WT and *Lrrtm3*-cKO mice. We found that the density of SPO puncta tended to be lower in SPB axons of *Lrrtm3*-cKO than of WT mice (*SI Appendix*, Fig. S6 *B* and *F*). Moreover, SPO puncta sizes in IPB axons were greater in *Lrrtm3*-cKO than in WT mice (*SI Appendix*, Fig. S6 *B* and *F*). However, the length of SPBs was specifically increased while the length of IPBs was significantly decreased in *Lrrtm3*-cKO mice, resulting in a slight decrease of the IPB/SPB ratio (*SI Appendix*, Fig. S6 *A* and *C–E*), an indicator of Mf maturation (41). Overall, these analyses suggest that LRRTM3 might contribute to the balanced projection of Mf bundles and be involved in the normal maturation of presynaptic axonal terminals projected to the CA3 area.

LRRTM3 Loss Remodels Apposed Thorny Excrescence Structures In Vivo. Mf presynaptic complexes connect DG granule neurons not only to glutamatergic CA3 pyramidal neurons but also to GABAergic interneurons (42). Because light microscopy is unable to precisely determine the involvement of LRRTM3 in connections between DG granule neuron axons and specific postsynaptic partner neurons (i.e., CA3 excitatory pyramidal neurons and GABAergic interneurons), serial block-face scanning electron microscopy (SBF-SEM) was performed to collect large datasets in the SL layer of the hippocampal CA3 subfield. This method was employed to analyze the Mf–CA3 circuitry at nanoscale resolution in transgenic mice (32, 42, 43). The volume for each image stack was 60 × 60 × 20 μm in the *x*, *y*, and *z* dimensions, and was composed of at least 400 serial images obtained at 50-nm thickness, resulting in a typical volume of 72,000 μm^3 (Movie S1). Eight proximal dendritic segments of CA3 pyramidal neurons were manually reconstructed. There were four segments per genotype, with mean linear dendritic lengths of 38.58 ± 3.37 μm per segment for WT and 40.45 ± 4.72 μm per segment for *Lrrtm3*-KO, running throughout their entire volumes including their TEs and corresponding MfBs. Note that conventional *Lrrtm3*-KO mice were used for SBF-SEM analyses, and major morphological issues were further addressed in *Lrrtm3*-cKO mice using transmission electron microscopy (TEM).

The density of MfBs along the proximal dendrites of CA3 neurons was also significantly lower in *Lrrtm3*-KO than in WT mice (Fig. 2 *A* and *C*). Subsequent morphological analyses of individual MfBs showed that the population means of MfB volume were significantly higher in *Lrrtm3*-KO mice (Fig. 2*D*). Representative MfBs taken every 10th percentile (in order of MfB volume) showed differences between the two genotypes in MfB size (Fig. 2 *B* and *D*). Notably, there were no differences in the number of synaptic contacts per MfB or the number of TEs per MfB between *Lrrtm3*-KO and WT mice (Fig. 2 *E* and *F*). To determine whether LRRTM3 deletions specifically affect Mf–CA3 TE synapses or the general integrity of other CA3 synapses, we analyzed SBF-SEM datasets of the SR layer of the CA3 region, just adjacent and distal to the SL layer. Dendritic segments of CA3 neurons in this layer mainly receive recurrent inputs from other CA3 neurons formed by association and commissural connections. Three-dimensional (3D) reconstruction of dendritic segments revealed no obvious between-group differences in mean dendritic spine density and PSD area (*SI Appendix*, Fig. S7 *A–C*).

TE density in hippocampal CA3 neurons was also lower in *Lrrtm3*-KO than in WT mice (Fig. 2 *G* and *I*). Individual TEs along the apical proximal dendritic segments of the hippocampal CA3 neurons were color-coded and separated from the dendritic shafts as discrete objects to facilitate subsequent morphological analyses (Fig. 2*H*). The population means of TE size showed no between-group differences (Fig. 2*J*). While the number of PSDs per TE volume was lower in *Lrrtm3*-KO (Fig. 2*K*), the number of MfBs per TE did not differ between genotypes (Fig. 2*L*), suggesting that the synaptic ratio between MfBs and CA3 TEs was similar in *Lrrtm3*-KO and WT mice. Importantly, the reduced density of Mf–CA3 synapses in *Lrrtm3*-KO mice was also confirmed in *Lrrtm3*-cKO mice (Fig. 2 *M* and *N*),

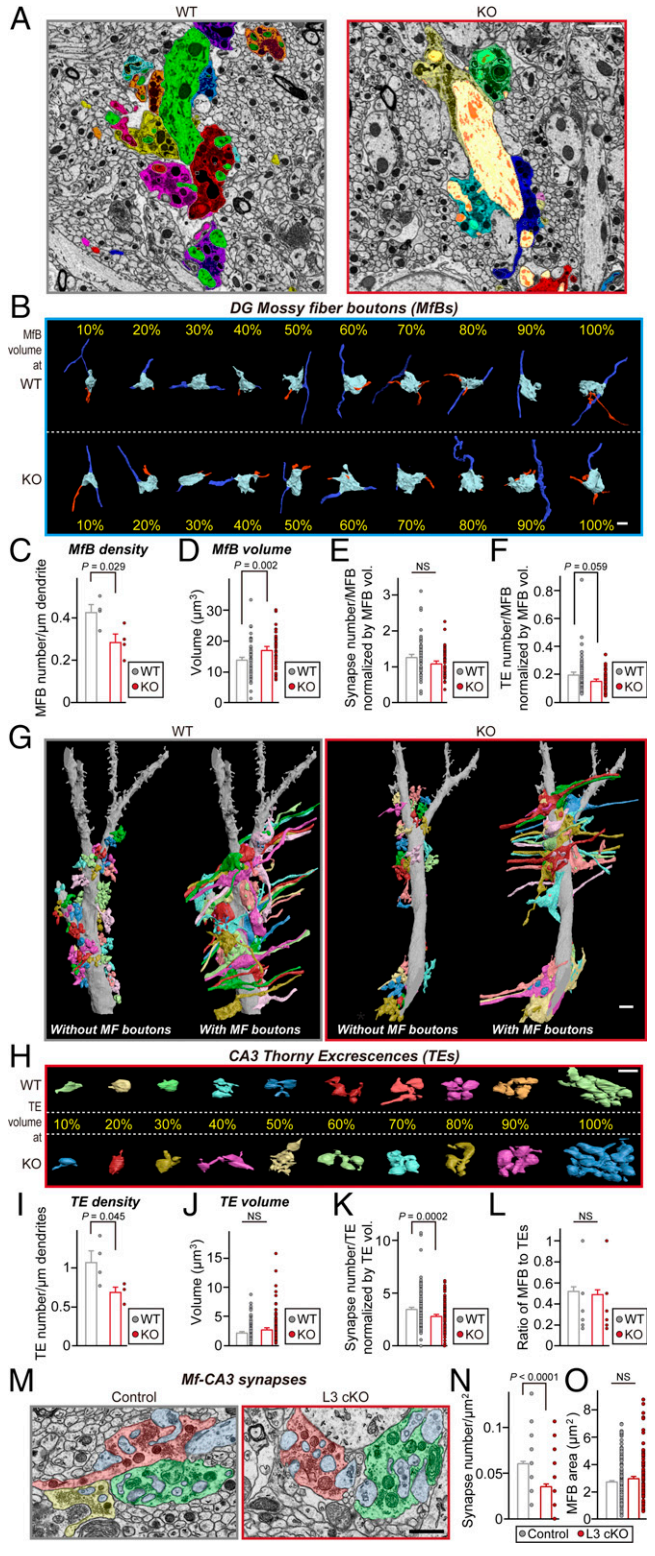

Fig. 2. Marked reduction of MfBs and CA3 TEs in LRRTM3-deficient mice. (*A*) Representative SBF-SEM images of Mf–CA3 synapses. CA3 dendritic segment innervated by MfBs is shown with manually segmented contours. Note the decreased number of MfBs in the *Lrrtm3*-KO mice. (Scale bar, 2 µm.) (*B*) MfBs at every 10th percentile in order of increasing MfB volume (Scale bar, 2 µm). Light sky blue, main MfB; blue, axonal fiber; orange, Mf filopodia. (*C*) Quantitation of MfB density (number of MfBs per micrometer dendrite length). Data represent means ± SEMs (n = 4 dendritic segments per group; Student's t test). (*D*) Mean of MfB volumes (WT, n = 66; KO, n = 43 MfBs; Student's t test). (*E*) Quantification of mean synapse numbers per MfB normalized by MfB volume (WT, n = 65; KO, n = 42 MfBs; Mann–Whitney U test). (*F*) Quantitation of TE density (number of TEs per MfB) normalized by MfB volume. Data represent means ± SEMs (WT, n = 64; KO, n = 42 MfBs; Mann–Whitney U test). (*G*) Representative 3D reconstruction of DG–CA3 synapses in WT and *Lrrtm3*-KO mice. The complex structures of individual TEs are displayed by showing the same dendritic segments with and without corresponding MfBs (Scale bar, 2 µm). (*H*) TEs at every 10th percentile in order of increasing TE volume. (Scale bar, 1 µm.) (*I*) Quantitation of TE density (number of TEs per micrometer dendrite length). Data are presented as means ± SEMs (n = 4 dendritic segments per group; Student's t test). (*J*) The mean value of TE volumes (WT, n = 164; KO, n = 114 TEs; Mann–Whitney U test). (*K*) Quantification of mean synapse numbers per TE normalized by TE volume (WT, n = 164; KO, n = 114 TEs; Mann–Whitney U test). (*L*) Quantitation of MfB ratio (number of MfBs per TE). Data are presented as means ± SEMs (WT, n = 65; KO, n = 42 MfBs; Mann–Whitney U test). (*M*) Representative TEM images of Mf–CA3 synapses. Areas marked in red/yellow/green and light sky-blue indicate presynaptic and postsynaptic sites, respectively (Scale bar, 2 µm). (*N*) Quantification of Mf–CA3 synaptic density (expressed as the number of Mf–CA3 synapses per square micrometer). Data represent means ± SEMs (n = 60 images from three mice per group; Mann–Whitney U test). (*O*) Mean of MfB areas (WT, n = 139; L3 cKO, n = 98; Mann–Whitney U test).

although the average MfB area in *Lrrtm3*-cKO mice was not different from that of control mice (Fig. 2*O*). Again, excitatory synaptic density and PSD length in the SR layer of the CA3 region were comparable in *Lrrtm3*-cKO and control mice (*SI Appendix*, Fig. S7 *D–F*). Collectively, these results indicate that LRRTM3 deletions selectively influence synaptic organization at DG–CA3 TE circuits, but not at CA3–CA3 recurrent connections.

LRRTM3 Loss Has No Effect on Mf Filopodial Synapse Structures. Because Kirrel3 was previously reported to participate in the formation of Mf filopodia to GABAergic neuron synapses (42) and IgSF8 was more recently reported to be involved in maintaining MF boutons and filopodial density (44), we assessed whether loss of LRRTM3 also affects connections at these particular synapses. Close examination of the presynaptic filopodia from the reconstructed MfBs showed that each individual MfB in adult WT mice possesses approximately two presynaptic filopodia, as previously reported (43). Further analyses showed that LRRTM3 deficiency significantly increased the mean number of Mf filopodia or branched filopodia per MfB, with no change in the length of individual Mf filopodia (*SI Appendix*, Fig. S8 *A–E*).

Mf filopodial synapses can be classified into three categories: 1) a synapse-free type, containing no presynaptic vesicle clusters or PSDs; 2) a partial synapse type, with clusters of synaptic vesicles but no visible PSDs; and 3) a complete synapse type, containing vesicle clusters adjacent to corresponding PSDs (42). Of these three categories of Mf filopodia, the partial synapse type constituted the highest percentage in both WT (81.3%) and *Lrrtm3*-KO (86.0%) mice (*SI Appendix*, Fig. S8*F*). We then determined the postsynaptic targets of Mf filopodial synapses. As expected, most complete synapse-type Mf filopodia were connected to nearby GABAergic neurons as postsynaptic targets (*SI Appendix*, Fig. S8 *A*, *B*, and *F*). Moreover, a few Mf filopodia formed synapses onto the dendritic shaft and TE of CA3 neurons (*SI Appendix*, Fig. S8 *C*, *D*, and *F*), which can be readily distinguished from GABAergic neurons by the presence of TEs in the dendrites of CA3 neurons. Although *Lrrtm3*-KO mice displayed more filopodia per MfB (*SI Appendix*, Fig. S8*E*), there were no differences between genotypes in the proportion of Mf filopodia in the three synaptic categories and in the percentage of their postsynaptic target cell types (*SI Appendix*, Fig. S8*F*), indicating that loss of LRRTM3 had little influence on Mf filopodial synapses.

NEUROSCIENCE

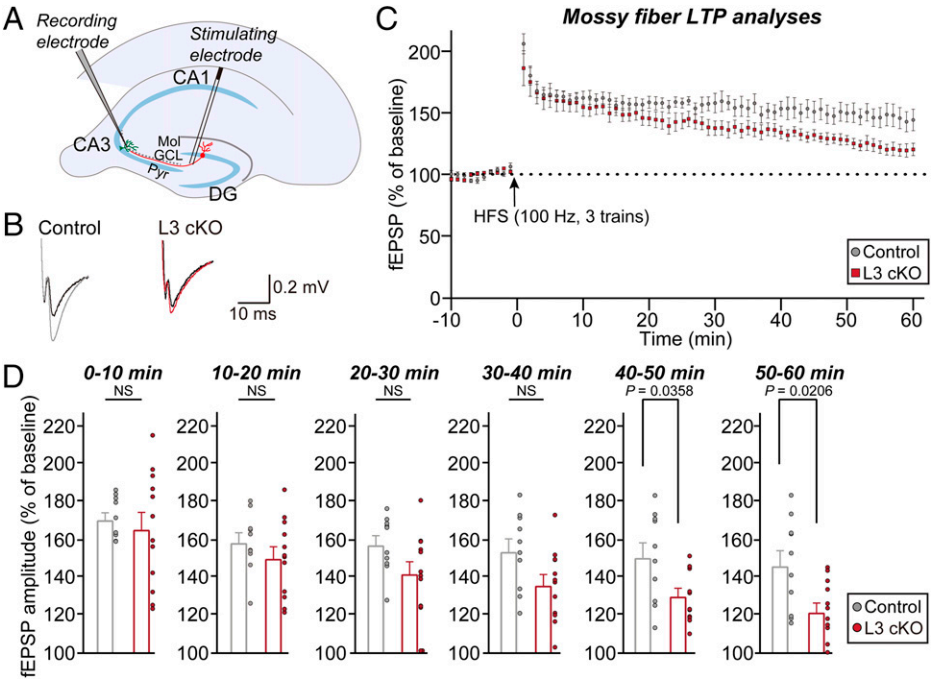

Fig. 3. Reduced maintenance of Mf-LTP in LRRTM3-deficient mice. (*A*) Schematic of an electrophysiological recording configuration showing stimulating sites in hippocampal DG and recording sites in hippocampal CA3 SR fields. (*B*) Representative average traces of field excitatory postsynaptic potentials (fEPSPs) evoked by stimulation of Mf before LTP induction by high-frequency stimulation (HFS) (black) and 50 to 60 min after LTP induction from control and *Lrrtm3*-cKO mice (light gray, control; red, L3 cKO). (*C*) fEPSP amplitudes plotted against Mf-LTP experiments as a function of recording time. An HFS (100 Hz, 1 s, three trains with a 10-s interval between trains) is given at the time indicated by the arrow. Data represent means ± SEMs (Mann–Whitney *U* test). (*D*) Quantification of fEPSP amplitudes in the Mf-LTP recording experiments. Data represent means ± SEMs (*n* denotes the number of analyzed slices; control, *n* = 10; L3 cKO, *n* = 12; Mann–Whitney *U* test).

LRRTM3 Is Required for Stabilization of Long-Term Potentiation at Mf–CA3 Synapses. We next performed patch-clamp recordings to examine whether the altered TEs and MfBs in *Lrrtm3*-cKO mice influenced the electrophysiological properties of CA3 pyramidal neurons. We first performed experiments in current-clamp mode using 500-ms current injection steps (from −100 to 250 pA in 25-pA increments), determining that firing rates of CA3 pyramidal neurons were comparable between control and *Lrrtm3*-cKO slices (*SI Appendix*, Fig. S9 *A* and *B*). To examine NMDA-EPSCs and AMPA-EPSCs from CA3 pyramidal neurons, we next performed whole-cell patch-clamp recordings by stimulating DG granule neurons. We found that NMDAR/AMPAR ratios in CA3 pyramidal neurons were similar in control and *Lrrtm3*-cKO mice (*SI Appendix*, Fig. S9 *C* and *D*). PPRs of Mf–CA3 synapses were also measured by stimulating DG granule neurons, but no detectable differences were found between control and *Lrrtm3*-cKO mice (*SI Appendix*, Fig. S9 *E* and *F*). These results indicate that conditional deletion of LRRTM3 in DG granule neurons does not affect the electrophysiological properties of CA3 pyramidal neurons under basal conditions.

We next examined whether LTP was altered when LRRTM3 was absent from Mf–CA3 synapses. Mf-LTP was induced by high-frequency tetanic stimulation (100 Hz for 1 s given three trains with a 10-s interval between trains) in the presence of the NMDAR antagonist, D-amino-5-phosphonopentanoic acid; this agent was used to prevent the responses from being contaminated by NMDAR-dependent LTP, which occurs at the associational/commissural synapses onto CA3 pyramidal neurons (45) (Fig. 3*A*). In both WT and *Lrrtm3*-cKO mice, tetanic stimulation elicited robust Mf-LTP (Fig. 3*B*). After tetanic stimulation, however, the magnitude of the LTP was significantly reduced in *Lrrtm3*-cKO mice (by ∼13% at 40 to 50 min and ∼17% at 50 to 60 min) (Fig. 3 *C* and *D*). These results indicate that LRRTM3 is required for the maintenance, but not the induction, of Mf-LTP.

LRRTM3 Coordinates Medial Entorhinal Cortical Inputs to the DG to Regulate Mf–CA3 Excitatory Synaptic Inputs and LTP. The above-described results collectively suggest that LRRTM3 might shape specific topographic architectures of MEC→DG and DG→CA3 circuits. However, it is unclear whether the activities of these two distinct neural circuits involving DG granule neurons are synchronized. To address this question, we attempted to specifically block neurotransmitter release at MPP–DG synapses and performed quantitative immunohistochemical analyses to monitor alteration of excitatory synapse structures in the DG and CA3 areas. To this end, we injected control and *Lrrtm3*-cKO mice with an AAV encoding an Flpo recombinase–mediated double-inverted open reading frame (fDIO), inverted enhanced green fluorescent protein (EGFP) and tetanus toxin (TeNT) gene (fDIO-TeNT-F2A-EGFP), or inverted EGFP alone (fDIO-F2A-EGFP) into the MEC, and a *trans*-neuronally transported version of Flpo fused to wheat germ agglutinin (WGA-Flpo) into the DG (Fig. 4*A*). This scheme allowed EGFP and TeNT to be expressed only after inversion of the double-floxed expression cassette in the MEC neurons by injecting AAVs coexpressing mCherry WGA-Flpo recombinases (Fig. 4*A*). We first validated whether expression of WGA-Flpo in the DG activated EGFP and TeNT expression in the MEC. We found that injection of WGA-Flpo AAV into the DG specifically induced EGFP expression in the MEC neurons and selectively reduced excitatory synaptic strength and neurotransmitter release at MPP–DG synapses (Fig. 4 *B*–*E*), validating the specific targeting of MEC projections. Neither the number of VGLUT1 puncta in the DG ML region nor the number of VGLUT1 puncta in SO and SR layers of CA3 was affected by inactivation of the MEC with TeNT in control mice

(Fig. 4 *F* and *G*), consistent with prior studies showing that glutamatergic transmission per se is dispensable for assembly of excitatory synapses (46, 47). Remarkably, presynaptic silencing of MEC–DG projections completely abrogated the loss of excitatory synaptic inputs onto the DG ML and CA3 SO and SR layers in *Lrrtm3*-cKO mice (Fig. 4 *F* and *G*). These results suggest that LRRTM3 may be essential for activity-dependent elimination or reformation in topographically connected hippocampal synapses, as similarly proposed for other paralogs [i.e., LRRTM1 and LRRTM2 (14)]. To test whether stimulation of MEC neuron activity could affect the number of excitatory synapses at the Mf–CA3 synapses of *Lrrtm3*-deficient neurons, we employed a chemogenetic approach to control the excitability of the MEC neurons (*SI Appendix*, Fig. S10). We injected Flpo-dependent AAVs expressing the designer receptor, Gq-coupled modified human M3 muscarinic receptor (AAV-fDIO-hM3Dq-mCherry [hM3Dq]), or a control (AAV-fDIO-mCherry) into the MEC, and further injected WGA-Flpo into the DG of WT and *Lrrtm3*-cKO mice (*SI Appendix*, Fig. S10*A*). Daily drinking water–based administration of the designer ligand, clozapine-*N*-oxide (CNO; 1 mg/kg), for 3 wk after Designer Receptors Exclusively Activated by Designer Drugs injections did not affect the number of VGLUT1 puncta in the DG and CA3 layers of WT mice but failed to rescue the deficits in excitatory synapse maintenance in DG and CA3 layers of LRRTM3-deficient neurons (*SI Appendix*, Fig. S10 *B–D*).

Finally, we examined whether the activity of MPP–DG synapses was involved in the maintenance of Mf-LTP (Fig. 4 *H–J*). TeNT expression in MPP–DG projections did not affect Mf-LTP in control mice but completely rescued the Mf-LTP impairment in *Lrrtm3*-cKO mice (Fig. 4 *H–J*). Strikingly, silencing MPP–DG circuit activities in *Lrrtm3*-cKO mice rescued the reduced excitability of DG granule neurons (Fig. 5 *A–C*). In contrast, CNO-mediated hM3Dq excitation of LRRTM3-deficient DG granule neurons failed to normalize the increase in neurotransmitter release (Fig. 5 *D–F*). These results suggest that increased neurotransmitter release in hippocampal DG granule neurons of *Lrrtm3*-cKO mice is likely coupled with reduced excitatory synaptic inputs and long-term plasticity. Collectively, our data demonstrate that LRRTM3 activity in the MEC projections onto DG granule neurons is involved in an activity-dependent excitatory synapse–remodeling process that is crucial for certain functions of DG–CA3 circuits.

Discussion

The best understood form of homeostatic plasticity arguably involves an up-regulation of presynaptic efficacy to counterbalance a reduction in postsynaptic neuron excitability (48). The current study showed that LRRTM3 is differentially involved at two interdependent hippocampal neural circuits, namely MPP–DG and DG–CA3 synapses, providing insights into a neural circuit–organizing role of LRRTM3 that involves a coordinated homeostatic presynaptic response.

Consistent with previous ISH analyses (21, 26, 35), we confirmed that the expressions of LRRTM3 are restricted to the DG granule neurons within the hippocampus, in contrast to the widespread expression of LRRTM1 and LRRTM2 in all hippocampal subfields. In an extension of our previous analyses on hippocampal DG synapses of *Lrrtm3*-KO mice, we first asked whether LRRTM3 is specifically involved in a particular PP. Our data showed that LRRTM3 is selectively required for assembly and/or maintenance of MEC projections to the DG pathway. We confirmed a subset of anatomical and electrophysiological phenotypes reported from constitutive *Lrrtm3*-KO mice (26) as also being observed after conditional postsynaptic KO of LRRTM3, with consistently reduced PP–DG LTP, excitability, and excitatory synaptic transmission in DG granule neurons, together with reduced excitatory synapse density in both DG granule neurons and CA3 pyramidal neurons. However, there were marked differences in sEPSCs and mEPSCs between constitutive and conditional *Lrrtm3*-KO mice. At present, the mechanistic basis of these differences is obscure, but developmental compensation, likely by reflecting differences in the timing of *Lrrtm3* deletion, is a possibility. Our hypothesis is that LRRTM3 expressed in proximal dendrites of DG granule neurons likely mediates specific recognition processes by interacting with an extracellular ligand(s) expressed in axons of MEC neurons. It remains to be determined, however, whether and how an LRRTM3 ligand(s) operates in a specific projection, which might be irrelevant of their specific localization/expression in the EC region. Regardless of LRRTM3's mechanism of action, our data establish that LRRTM3 acts as a critical factor in conferring the properties of a defined specific neural circuit.

Upon deletion of LRRTM3 at Mf–CA3 synapses, we made a series of observations that were initially unexpected and surprising. Importantly, high-resolution ultrastructural analyses showed that loss of LRRTM3 specifically reduced the density of Mf–CA3 synapses in proximal dendrites of both conventional and conditional *Lrrtm3*-deficient mice in vivo. Paradoxically, the sizes of the MfBs were increased in *Lrrtm3*-KO, but not in *Lrrtm3*-cKO, mice. This discrepancy may result from differences in genetic deletion strategies or the potential absence of developmental compensation in *Lrrtm3*-cKO mice. The presence of these structural alterations in *Lrrtm3*-deficient mice suggests that LRRTM3 loss influences inputs onto CA3 neurons (i.e., by presynaptic deletion effects) or exerts homeostatic adjustment in a downstream region of the connected hippocampal circuits. To discriminate between these possibilities, the exact localization of LRRTM3 should be determined with high-resolution approaches. Because our in-house and currently available commercial LRRTM3-specific antibodies were not suitable for immunohistochemical analyses to determine the precise localization of this protein at synapses in vivo, it remains unclear if a fraction of LRRTM3 might be expressed in the terminals of DG granular axons in vivo. Notably, LRRTM4 is presynaptically localized to retinal bipolar cells (27, 49). Nevertheless, based on various prior results related to LRRTM family members at hippocampal synapses (11, 12), we favor the latter possibility that LRRTM3 likely regulates the homeostatic synaptic plasticity that occurs predominantly at proximal synapses between DG and CA3 neurons (31, 50). The morphological alterations of DG Mf and CA3 TEs are likely due to homeostatic adaptations, driven by reduced inputs from MPPs and functioning to balance excitatory and inhibitory network activity in the hippocampus. There was no difference in density or PSD area of distal dendrites of CA3 pyramidal neurons derived from *Lrrtm3*-KO and WT mice.

LRRTM3 is dispensable for development of Mf filopodia–CA3 pyramidal neuron synapses, although the proportion of these synapses was much lower (~0.9%) in juvenile postnatal day (P)42 WT and *Lrrtm3*-KO mice than in P14 WT mice (~5.2%) (42). These data suggest that different sets of cell-surface proteins are involved in organizing the structural projections of DG Mf to distinct postsynaptic targets (i.e., LRRTM3 targeting CA3 pyramidal neurons, Kirrel3 targeting GABAergic interneurons, and IgSF8 targeting DG, CA3, and GABAergic interneurons) (33, 44). The number of Mf filopodia was significantly higher in *Lrrtm3*-KO mice than in WT mice, although there was no difference in the length of their Mf filopodia. In contrast, *Lrrtm3*-KO mice exhibited a comparable number of complete synapses with GABAergic

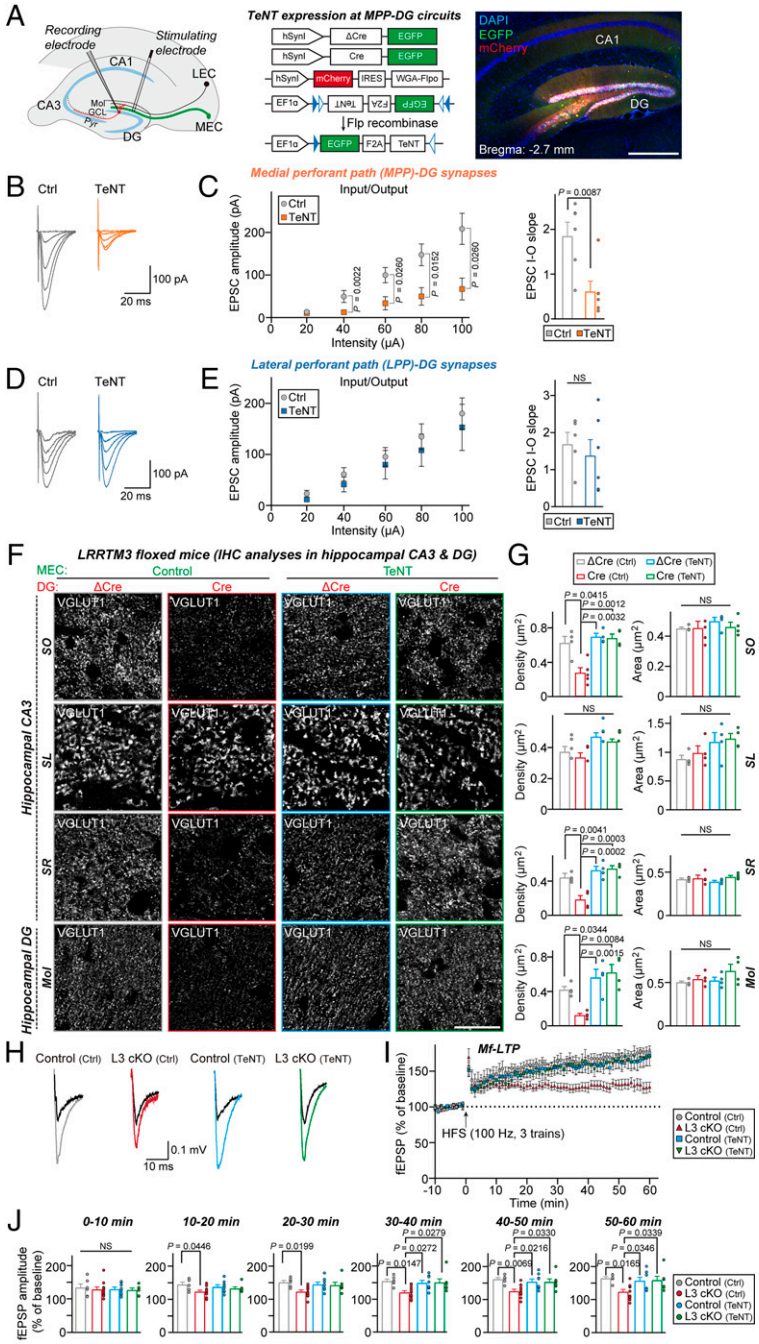

Fig. 4. Impaired excitatory synapse refinement and Mf-LTP in LRRTM3-deficient mice are rescued by blocking synaptic transmission at MPP–DG synapses. (*A*) Design of AAVs used to inactivate neurotransmitter release from MEC neurons to DG granule neurons. Double-floxed inverted TeNT-AAV (2xFlx-TeNT-AAV) encodes a bicistronic expression encoding EGFP (for visualizing infected MEC neurons) and TeNT (to block synaptic transmission). The coding region of the double-floxed inverted TeNT-AAV is not translated until Flpo recombinase flips the inverted coding region into the correct orientation. WGA-Flpo AAV mediates bicistronic expression of mCherry and WGA-Flpo. When this AAV infects DG neurons, WGA-Flpo is *trans*-neuronally transferred to connected MEC neurons, whereas mCherry is only expressed in the infected DG neurons. (Scale bar, 100 μm.) (*B* and *C*) Measurements of excitatory synaptic strength via I-O curves of control- and TeNT-expressing WT mice, presenting representative AMPAR-EPSC traces (*B*), summary plotting of the EPSC amplitudes as a function of MPP stimulation current (*C*, *Left*), and summary graph of fitted linear I-O slopes (*C*, *Right*). Data represent means ± SEMs (*n* denotes the number of recorded neurons; control, $n = 10$; TeNT, $n = 11$; Mann–Whitney *U* test). (*D* and *E*) Same as *B* and *C*, except that AMPAR-EPSCs were recorded in the same neurons as in *B* and *C* as a function of LPP stimulation. Data represent means ± SEMs (*n* denotes the number of recorded neurons; control, $n = 8$; TeNT, $n = 9$; Mann–Whitney *U* test). (*F* and *G*) Representative immunofluorescence images (*F*) and quantification (*G*) of VGLUT1 puncta density. Data shown are means ± SEMs (*n* denotes the number of analyzed mice; ΔCre [Ctrl], $n = 4$; Cre [Ctrl], $n = 4$; ΔCre [TeNT], $n = 4$; Cre [TeNT], $n = 4$ mice; ANOVA followed by Shapiro–Wilk normality test). (Scale bar, 20 μm.) IHC, immunohistochemistry. (*H*) Representative average traces of fEPSPs, evoked in WT and *Lrrtm3*-cKO mice injected with either control or TeNT by stimulation of Mf before LTP induction by HFS (black) and 50 to 60 min after LTP induction (light gray, control [Ctrl]; red, L3 cKO [Ctrl]; blue, control [TeNT]; green, L3 cKO [TeNT]). (*I*) fEPSP amplitudes plotted against Mf-LTP experiments as a function of recording time. An HFS (100 Hz, three 1-s trains at 10-s intervals) is given at the time indicated by the arrow. Data represent means ± SEMs. (*J*) Quantification of fEPSP amplitudes in the Mf-LTP recording experiments. Data represent means ± SEMs (*n* denotes the number of analyzed slices; WT [Ctrl], $n = 6$; WT [TeNT], $n = 8$; L3 cKO [Ctrl], $n = 11$; L3 cKO [TeNT], $n = 7$; nonparametric ANOVA with post hoc Tukey's multiple-comparison test).

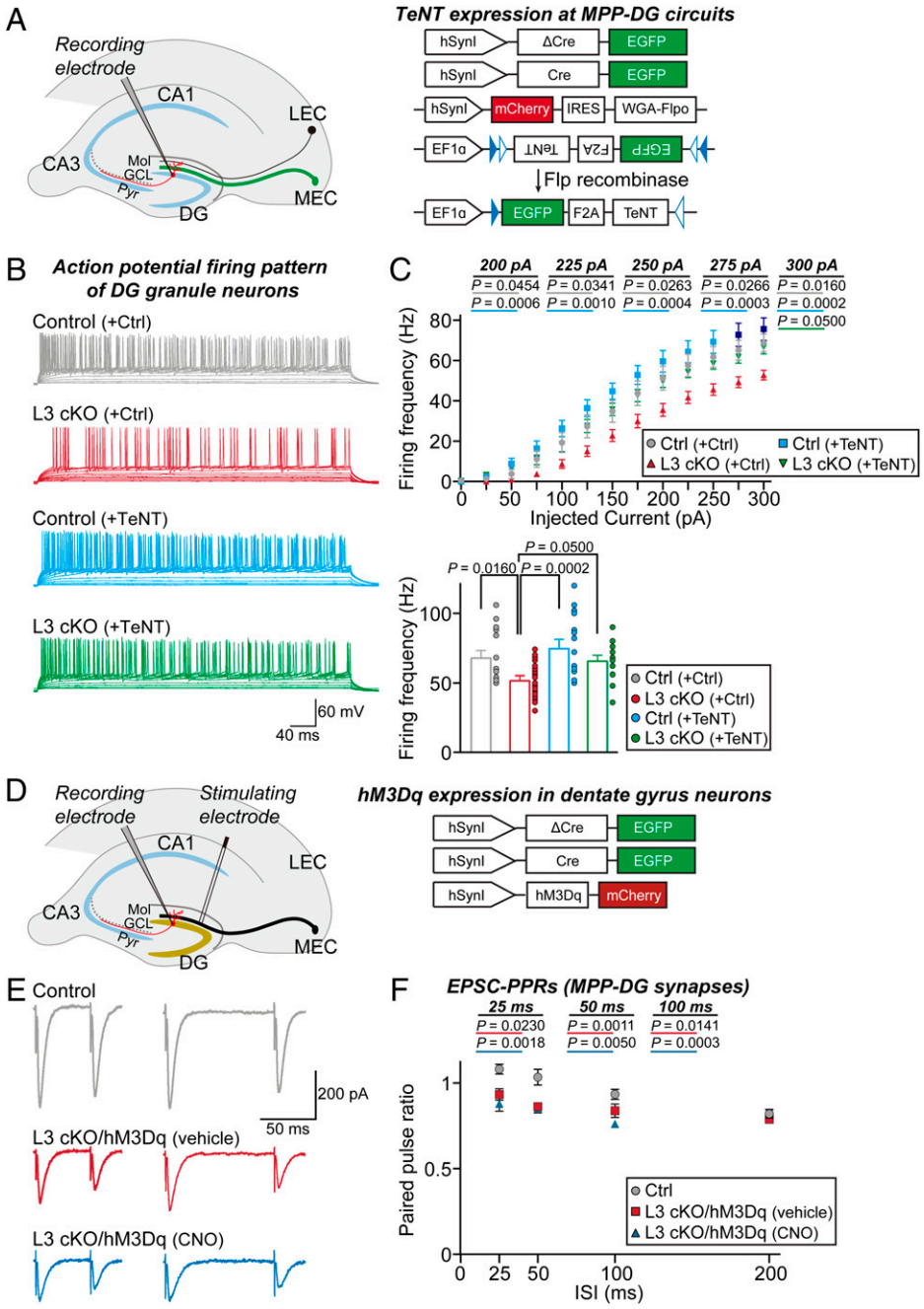

Fig. 5. Action of LRRTM3 in regulating excitatory synaptic transmission at MPP–DG synapses is a prerequisite for synchronized activity-dependent circuit properties. (*A*) Design of AAVs used to inactivate neurotransmitter release from MEC neurons to DG granule neurons. Double-floxed inverted TeNT-AAV (2xFlx-TeNT-AAV) encodes a bicistronic expression construct encoding EGFP (for visualizing infected MEC neurons) and TeNT (to block synaptic transmission). The coding region of the double-floxed inverted TeNT-AAV is not translated until the Flpo recombinase flips the inverted coding region into the correct orientation. WGA-Flpo AAV mediates bicistronic expression of mCherry and WGA-Flpo. Upon infection of DG neurons with this AAV, WGA-Flpo is *trans*-neuronally transferred to connected MEC neurons, whereas mCherry is only expressed in the infected DG neurons. (*B* and *C*) Representative traces (*B*), summary graphs (*C*, *Top*), and average (*C*, *Bottom*) of intrinsic excitability measured as firing rates in response to step depolarizing currents (duration, 500 ms) in DG granule neurons. Individual points represent means ± SEMs (*n* denotes the number of recorded neurons; control, $n = 16$; control [+TeNT], $n = 16$; L3 cKO, $n = 26$; L3 cKO [+TeNT], $n = 16$; ANOVA followed by Tukey's post hoc test after Shapiro–Wilk normality test). (*D*) Schematic of an electrophysiological recording configuration showing stimulating and recording sites in hippocampal CA3. (*E*) Representative traces of PPRs of EPSCs at MPP–DG synapses at two different interstimulus intervals (50 and 100 ms). (*F*) Average of EPSC-PPRs at MPP–DG synapses at four different interstimulus intervals (25, 50, 100, and 200 ms). Data represent means ± SEMs (*n* denotes the number of recorded neurons; control, $n = 20$; L3 cKO+hM3Dq [vehicle], $n = 16$; L3 cKO+hM3Dq [CNO], $n = 12$; nonparametric ANOVA with Kruskal–Wallis test followed by post hoc Dunn's multiple-comparison test).

interneurons. The cause for the increased number of Mf filopodia upon LRRTM3 deletion is currently unclear, although LRRTM3 loss in the Mf filopodia and/or GABAergic interneurons may concertedly drive this structural rearrangement. Notably, presynaptic neurotransmitter release was increased at MPP–DG synapses of LRRTM3-deficient neurons, but not at Mf–CA3 synapses. Presynaptic silencing of MEC neurons at MPP–DG synapses blunted the effects of LRRTM3

deletion on DG granule neuron excitability or excitatory synaptic inputs and LTP at Mf–CA3 synapses. Our interpretation of these results is that the elimination of excitatory synapses at MPP–DG synapses triggered by LRRTM3 loss activates a homeostatic presynaptic response, as recently shown in an autaptic circuit (51), that further drives activation of the molecular machinery involved in excitatory synapse refinement. Nlgn1 was shown to modulate presynaptic release probability in hippocampal CA1 synapses, likely through Nrxns (52). Given that these Nlgn1 and LRRTM3 loss-of-function phenotypes and the analyzed neural circuits are distinct, a complete understanding of *trans*-synaptic effects on presynaptic functions will require further investigation into what dictates how LRRTM3 deletion induces the homeostatic presynaptic response. Loss of LRRTM3 also reduced the excitability of DG granule neurons, but not one of the CA3 neurons; instead, it significantly reduced excitatory synapse development in a subset of CA3 layers. Intriguingly, chemogenetic activation of DG granule neurons rescued the deficits in excitatory synapse maintenance in DG and CA3 areas, but did not rescue the impaired maintenance of Mf-LTP and failed to normalize the increase in neurotransmitter release at MPP–DG synapses (Fig. 5 and *SI Appendix*, Fig. S11). Thus, our observations suggest that LRRTM3 deletions induce an alteration or dysregulation of homeostatic plasticity and excitatory synaptic properties that are distinctively manifested at two different hippocampal circuits, and that LRRTM3 acts primarily at a postsynaptic locus in the MPP–DG circuit, with its actions likely propagating to the DG–CA3 circuit to regulate specific excitatory synapse properties. More sophisticated experiments will be required to discern the temporal order of various biological phenomena documented in the present study.

Although no published study has reported behavioral analyses of LRRTM3-deficient mice, it is plausible to speculate that LRRTM3 might be involved in a subset of cognitive tasks that are mediated by neural circuits involving the DG (53, 54), and other DG-linked regions (55, 56). Structural plasticity in Mf neural circuits was previously reported to be associated with long-lasting memory (57, 58), with LTP inducing Mf growth and remodeling (59, 60). Moreover, molecular profiles in Mf terminals are dynamically regulated when induced by spatial learning (61, 62). Future studies using various transgenic animals with similar structural and functional features should elucidate how the information flow in hippocampal circuits is carried to downstream structures involved in governing cognitive tasks.

In summary, the present study delineated the in vivo role of LRRTM3 in organizing the specific topography of hippocampal synaptic connections and the activity-dependent refinement of excitatory synapses for discrete granule cell activity.

Materials and Methods

Animals. All mice were maintained and handled in accordance with protocols (DGIST-IACUC-19052109-00) approved by the Institutional Animal Care and Use Committee of DGIST under standard, temperature-controlled laboratory conditions. Mice were kept on a 12:12 light/dark cycle (lights on at 7:00 AM), and received water and food ad libitum. Constitutive *Lrrtm3*-KO mice were described previously (26). LRRTM3-cKO mice were generated at Biocytogen. Floxed LRRTM3 (*Lrrtm3*$^{f/f}$) mice were generated by flanking exons 1 and 2 with loxP sites (*SI Appendix*, Fig. S2). In detail, *Lrrtm3* floxed mice were generated using an embryonic stem cell (ESC)–based gene-targeting method. The CCDS35925 transcript of the *Lrrtm3* gene was used in designing a targeting vector into which a loxP site was introduced ~2 kb upstream of the 5′ untranslated region of the *Lrrtm3* gene. The FRT site, neomycin resistance gene, and second loxP site were inserted in introns 2 and 3 of the *Lrrtm3* gene. This arrangement positions loxP sites to direct Cre-mediated deletion of the *Lrrtm3* allele. A diphtheria toxin minigene was inserted for negative selection. ESC culture and selection for homologous recombination were performed using a C57BL/6 mouse ESC line. The targeting vector was introduced into C57BL/6 mouse ESCs by electroporation. Positive ESC clones, identified by screening for successful recombination of the target DNA, were injected into C57BL/6 mouse blastocysts. Blastocysts were then implanted into host mice, resulting in chimeras. Chimeras were bred with strains of an Flp mouse strain to remove the neomycin resistance cassette and produce mice with germline transmission of the target gene. Mice were maintained in the C57BL/6N background. All experimental procedures were performed on male mice, using a littermate control without Cre expression. Mouse genotyping for constitutive *Lrrtm3*-KO mice was previously described (26).

Antibodies. The following primary antibodies were generated in the laboratory of Jaewon Ko: guinea pig polyclonal anti–pan-LRRTM3 (JK132; RRID: AB_2810943). Synthesized peptides of mouse LRRTM3 (amino acids 564 to 582; DLSTITSAGRISDHKPQLA) were conjugated with keyhole limpet hemocyanin, and injected three times into guinea pigs. Antisera were collected and affinity-purified using SulfoLink columns (Pierce), onto which the same conjugated peptide had been immobilized. Commercially purchased antibodies included rabbit polyclonal anti-SPO (Synaptic Systems; RRID: AB_887841), guinea pig polyclonal anti-VGLUT1 (Sigma-Aldrich; RRID: AB_2301751), rabbit polyclonal anti-VGAT (Synaptic Systems; RRID: AB_887869), mouse monoclonal anti-LRRTM4 (clone N205B/22; NeuroMab; RRID: AB_10674105), and mouse monoclonal anti–β-actin (clone C4; Santa Cruz Biotechnology; RRID: AB_626632).

Plasmids. The AAV vectors were generated by standard molecular biology procedures as follows: AAV-EF1α-fDIO-EGFP-F2A-TeNT was constructed by PCR amplification of the EGFP-F2A-TeNT segment using the pAAV-2xFlx-TeNT (63) plasmid as a template; the product was digested with *Asc*I and *Nhe*I, and subcloned into the pAAV-EF1α-fDIO-EYFP vector (Addgene; 55641). AAV-EF1α-fDIO-EGFP-F2A was constructed by PCR amplification of the EGFP-F2A segment, which was performed similar to the above-described generation of AAV-EF1α-fDIO-EGFP-F2A-TeNT. AAV-EF1α-fDIO-EGFP-F2A-hM3Dq was constructed by PCR amplification of the hM3Dq sequence from the pAAV-hSyn-DIO-HA-hM3D(Gq)-IRES-mCitrine vector (Addgene; 50454); the product was digested with *Asc*I, and subcloned into the pAAV-EF1α-fDIO-EYFP-F2A vector. AAV-phSyn-WGA-IRES-mCherry-Flpo-bGHpA was constructed by PCR amplification of the WGA-IRES-mCherry segment from pAAV-WGA-Cre-IRES-mCherry (64); the product was digested with *Kpn*I and *Hind*III, and subcloned into the pAAV-phSyn(S)-Flpo-bGHpA vector (Addgene; 51669). pAAV-hSyn-hM3Dq-mCherry was purchased (Addgene; 50474). The following plasmids were as previously described: AAV-WGA-ΔCre-IRES-tdTomato and AAV-WGA-Cre-IRES-tdTomato (64), and pAAV-2xFlx-TetTox (63).

Also see *SI Appendix, Materials and Methods* for details for fluorescence in situ hybridization (RNAscope assay), immunocytochemistry, confocal microscopy imaging, preparation of AAVs and titration, stereotactic surgery, electrophysiology, tissue processing for SBF-SEM and TEM, acquisition of SBF-SEM datasets and 3D reconstruction, sterology, physical dissector counting, and chemogenetics experiments.

Experimental Design and Statistical Analysis. All statistical analyses were performed using GraphPad Prism 7 software (RRID: SCR_002798). The normality of distributed data was determined using the Shapiro–Wilk normality test. Normally distributed data were compared using Student's *t* test or the ANOVA test, and nonnormally distributed data were compared by the Mann–Whitney *U* test, nonparametric ANOVA with Kruskal–Wallis test followed by post hoc Dunn's multiple-comparison test, or nonparametric ANOVA with post hoc Tukey's multiple-comparison test. If a single value made the data distribution nonnormal and was found to be a significant outlier ($P < 0.05$) by Grubb's test, it was regarded as an outlier. Dataset S1 presents detailed statistics.

Data Availability. All study data are included in the article and supporting information.

ACKNOWLEDGMENTS. We thank Jinha Kim (DGIST) for technical assistance, Dr. Soo-Jeong Kim for initial analyses, various KBRI personnel (Chan Hee Lee, Na Young Do, Hyun Jib Jang, Bo Kyeom Bae, and Mi Ji Kim) for technical support with electron microscopy image segmentation, and Dr. Nobuhiko Ohno (Jichi Medical University, Japan) for the gift of Ketjen black powder. This study was supported by grants from the Ministry for Health and Welfare Affairs (HI17C0080 to J. Ko), National Research Foundation of Korea, funded by the Ministry of Science and ICT (2017M3C7A1023470 to J. Ko), KBRI Basic Research Program funded by the Ministry of Science and ICT (19-BR-01-01 to K.J.L.), and DGIST R&D Program of the Ministry of Science, ICT & Future Planning (21-CoE-BT-01 to J.S., J.W.U., and J. Ko).

1. G. Condomitti, J. de Wit, Heparan sulfate proteoglycans as emerging players in synaptic specificity. *Front. Mol. Neurosci.* **11**, 14 (2018).
2. D. Park, S. Bae, T. H. Yoon, J. Ko, Molecular mechanisms of synaptic specificity: Spotlight on hippocampal and cerebellar synapse organizers. *Mol. Cells* **41**, 373–380 (2018).
3. T. C. Südhof, Towards an understanding of synapse formation. *Neuron* **100**, 276–293 (2018).
4. T. Biederer, P. S. Kaeser, T. A. Blanpied, Transcellular nanoalignment of synaptic function. *Neuron* **96**, 680–696 (2017).
5. T. C. Südhof, Synaptic neurexin complexes: A molecular code for the logic of neural circuits. *Cell* **171**, 745–769 (2017).
6. D. S. Berns, L. A. DeNardo, D. T. Pederick, L. Luo, Teneurin-3 controls topographic circuit assembly in the hippocampus. *Nature* **554**, 328–333 (2018).
7. G. R. Anderson *et al.*, Postsynaptic adhesion GPCR latrophilin-2 mediates target recognition in entorhinal-hippocampal synapse assembly. *J. Cell Biol.* **216**, 3831–3846 (2017).
8. M. E. Williams, J. de Wit, A. Ghosh, Molecular mechanisms of synaptic specificity in developing neural circuits. *Neuron* **68**, 9–18 (2010).
9. L. Y. Chen, M. Jiang, B. Zhang, O. Gokce, T. C. Südhof, Conditional deletion of all neurexins defines diversity of essential synaptic organizer functions for neurexins. *Neuron* **94**, 611–6254 (2017).
10. L. M. Richter, J. Gjorgjieva, Understanding neural circuit development through theory and models. *Curr. Opin. Neurobiol.* **46**, 39–47 (2017).
11. J. Ko, The leucine-rich repeat superfamily of synaptic adhesion molecules: LRRTMs and Slitrks. *Mol. Cells* **34**, 335–340 (2012).
12. R. T. Roppongi, B. Karimi, T. J. Siddiqui, Role of LRRTMs in synapse development and plasticity. *Neurosci. Res.* **116**, 18–28 (2017).
13. J. Ko, M. V. Fuccillo, R. C. Malenka, T. C. Südhof, LRRTM2 functions as a neurexin ligand in promoting excitatory synapse formation. *Neuron* **64**, 791–798 (2009).
14. J. Ko, G. J. Soler-Llavina, M. V. Fuccillo, R. C. Malenka, T. C. Südhof, Neuroligins/LRRTMs prevent activity- and Ca^{2+}/calmodulin-dependent synapse elimination in cultured neurons. *J. Cell Biol.* **194**, 323–334 (2011).
15. G. J. Soler-Llavina, M. V. Fuccillo, J. Ko, T. C. Südhof, R. C. Malenka, The neurexin ligands, neuroligins and leucine-rich repeat transmembrane proteins, perform convergent and divergent synaptic functions in vivo. *Proc. Natl. Acad. Sci. U.S.A.* **108**, 16502–16509 (2011).
16. G. J. Soler-Llavina *et al.*, Leucine-rich repeat transmembrane proteins are essential for maintenance of long-term potentiation. *Neuron* **79**, 439–446 (2013).
17. M. Bhouri *et al.*, Deletion of *LRRTM1* and *LRRTM2* in adult mice impairs basal AMPA receptor transmission and LTP in hippocampal CA1 pyramidal neurons. *Proc. Natl. Acad. Sci. U.S.A.* **115**, E5382–E5389 (2018).
18. M. W. Linhoff *et al.*, An unbiased expression screen for synaptogenic proteins identifies the LRRTM protein family as synaptic organizers. *Neuron* **61**, 734–749 (2009).
19. J. de Wit *et al.*, LRRTM2 interacts with Neurexin1 and regulates excitatory synapse formation. *Neuron* **64**, 799–806 (2009).
20. T. J. Siddiqui, R. Pancaroglu, Y. Kang, A. Rooyakkers, A. M. Craig, LRRTMs and neuroligins bind neurexins with a differential code to cooperate in glutamate synapse development. *J. Neurosci.* **30**, 7495–7506 (2010).
21. J. de Wit *et al.*, Unbiased discovery of glypican as a receptor for LRRTM4 in regulating excitatory synapse development. *Neuron* **79**, 696–711 (2013).
22. J. S. Ko *et al.*, PTPσ functions as a presynaptic receptor for the glypican-4/LRRTM4 complex and is essential for excitatory synaptic transmission. *Proc. Natl. Acad. Sci. U.S.A.* **112**, 1874–1879 (2015).
23. A. Yamagata *et al.*, Structural insights into modulation and selectivity of transsynaptic neurexin-LRRTM interaction. *Nat. Commun.* **9**, 3964 (2018).
24. R. T. Roppongi *et al.*, LRRTMs organize synapses through differential engagement of neurexin and PTPσ. *Neuron* **106**, 108–125 (2020).
25. K. A. Han *et al.*, LAR-RPTPs directly interact with neurexins to coordinate bidirectional assembly of molecular machineries. *J. Neurosci.* **40**, 8438–8462 (2020).
26. J. W. Um *et al.*, LRRTM3 regulates excitatory synapse development through alternative splicing and neurexin binding. *Cell Rep.* **14**, 808–822 (2016).
27. R. Sinha *et al.*, LRRTM4: A novel regulator of presynaptic inhibition and ribbon synapse arrangements of retinal bipolar cells. *Neuron* **105**, 1007–1017 (2020).
28. R. L. Rawson, E. A. Martin, M. E. Williams, Mechanisms of input and output synaptic specificity: Finding partners, building synapses, and fine-tuning communication. *Curr. Opin. Neurobiol.* **45**, 39–44 (2017).
29. G. G. Turrigiano, The dialectic of Hebb and homeostasis. *Philos. Trans. R. Soc. Lond. B Biol. Sci.* **372**, 20160258 (2017).
30. L. Acsády, A. Kamondi, A. Sík, T. Freund, G. Buzsáki, GABAergic cells are the major postsynaptic targets of mossy fibers in the rat hippocampus. *J. Neurosci.* **18**, 3386–3403 (1998).
31. K. J. Lee *et al.*, Mossy fiber-CA3 synapses mediate homeostatic plasticity in mature hippocampal neurons. *Neuron* **77**, 99–114 (2013).
32. F. J. Weng *et al.*, Npas4 is a critical regulator of learning-induced plasticity at mossy fiber-CA3 synapses during contextual memory formation. *Neuron* **97**, 1137–1152.e5 (2018).
33. E. A. Martin *et al.*, The intellectual disability gene Kirrel3 regulates target-specific mossy fiber synapse development in the hippocampus. *eLife* **4**, e09395 (2015).
34. K. A. Park *et al.*, Excitatory synaptic drive and feedforward inhibition in the hippocampal CA3 circuit are regulated by SynCAM 1. *J. Neurosci.* **36**, 7464–7475 (2016).
35. J. Laurén, M. S. Airaksinen, M. Saarma, T. Timmusk, A novel gene family encoding leucine-rich repeat transmembrane proteins differentially expressed in the nervous system. *Genomics* **81**, 411–421 (2003).
36. T. J. Siddiqui *et al.*, An LRRTM4-HSPG complex mediates excitatory synapse development on dentate gyrus granule cells. *Neuron* **79**, 680–695 (2013).
37. X. Sun *et al.*, Functionally distinct neuronal ensembles within the memory engram. *Cell* **181**, 410–423 (2020).
38. M. P. Witter, The perforant path: Projections from the entorhinal cortex to the dentate gyrus. *Prog. Brain Res.* **163**, 43–61 (2007).
39. H. E. Scharfman, C. E. Myers, Hilar mossy cells of the dentate gyrus: A historical perspective. *Front. Neural Circuits* **6**, 106 (2013).
40. D. G. Amaral, J. A. Dent, Development of the mossy fibers of the dentate gyrus: I. A light and electron microscopic study of the mossy fibers and their expansions. *J. Comp. Neurol.* **195**, 51–86 (1981).
41. E. A. Rudnitskaya *et al.*, Features of postnatal hippocampal development in a rat model of sporadic Alzheimer's disease. *Front. Neurosci.* **14**, 533 (2020).
42. E. A. Martin, D. Woodruff, R. L. Rawson, M. E. Williams, Examining hippocampal mossy fiber synapses by 3D electron microscopy in wildtype and Kirrel3 knockout mice. *eNeuro* **4**, ENEURO.0088-17.2017 (2017).
43. S. A. Wilke *et al.*, Deconstructing complexity: Serial block-face electron microscopic analysis of the hippocampal mossy fiber synapse. *J. Neurosci.* **33**, 507–522 (2013).
44. N. Apóstolo *et al.*, Synapse type-specific proteomic dissection identifies IgSF8 as a hippocampal CA3 microcircuit organizer. *Nat. Commun.* **11**, 5171 (2020).
45. R. A. Nicoll, D. Schmitz, Synaptic plasticity at hippocampal mossy fibre synapses. *Nat. Rev. Neurosci.* **6**, 863–876 (2005).
46. R. Sando *et al.*, Assembly of excitatory synapses in the absence of glutamatergic neurotransmission. *Neuron* **94**, 312–321 (2017).
47. M. Verhage *et al.*, Synaptic assembly of the brain in the absence of neurotransmitter secretion. *Science* **287**, 864–869 (2000).
48. J. Burrone, M. O'Byrne, V. N. Murthy, Multiple forms of synaptic plasticity triggered by selective suppression of activity in individual neurons. *Nature* **420**, 414–418 (2002).
49. M. A. Agosto, T. G. Wensel, LRRTM4 is a member of the transsynaptic complex between rod photoreceptors and bipolar cells. *J. Comp. Neurol.* **529**, 221–233 (2021).
50. S. Chierzi, T. J. Stachniak, E. Trudel, C. W. Bourque, K. K. Murai, Activity maintains structural plasticity of mossy fiber terminals in the hippocampus. *Mol. Cell. Neurosci.* **50**, 260–271 (2012).
51. C. D. Velasco, A. Llobet, Synapse elimination activates a coordinated homeostatic presynaptic response in an autaptic circuit. *Commun. Biol.* **3**, 260 (2020).
52. K. Futai *et al.*, Retrograde modulation of presynaptic release probability through signaling mediated by PSD-95-neuroligin. *Nat. Neurosci.* **10**, 186–195 (2007).
53. T. J. McHugh *et al.*, Dentate gyrus NMDA receptors mediate rapid pattern separation in the hippocampal network. *Science* **317**, 94–99 (2007).
54. B. E. Bernier *et al.*, Dentate gyrus contributes to retrieval as well as encoding: Evidence from context fear conditioning, recall, and extinction. *J. Neurosci.* **37**, 6359–6371 (2017).
55. R. R. Rozeske *et al.*, Prefrontal-periaqueductal gray-projecting neurons mediate context fear discrimination. *Neuron* **97**, 898–910 (2018).
56. A. Grosso, G. Santoni, E. Manassero, A. Renna, B. Sacchetti, A neuronal basis for fear discrimination in the lateral amygdala. *Nat. Commun.* **9**, 1214 (2018).
57. D. A. Henze, N. N. Urban, G. Barrionuevo, The multifarious hippocampal mossy fiber pathway: A review. *Neuroscience* **98**, 407–427 (2000).
58. I. Galimberti *et al.*, Long-term rearrangements of hippocampal mossy fiber terminal connectivity in the adult regulated by experience. *Neuron* **50**, 749–763 (2006).
59. V. Ramírez-Amaya, I. Balderas, J. Sandoval, M. L. Escobar, F. Bermúdez-Rattoni, Spatial long-term memory is related to mossy fiber synaptogenesis. *J. Neurosci.* **21**, 7340–7348 (2001).
60. A. Routtenberg, Adult learning and remodeling of hippocampal mossy fibers: Unheralded participant in circuitry for long-lasting spatial memory. *Hippocampus* **20**, 44–45 (2010).
61. M. R. Holahan, J. L. Rekart, J. Sandoval, A. Routtenberg, Spatial learning induces presynaptic structural remodeling in the hippocampal mossy fiber system of two rat strains. *Hippocampus* **16**, 560–570 (2006).
62. R. McGonigal, N. Tabatadze, A. Routtenberg, Selective presynaptic terminal remodeling induced by spatial, but not cued, learning: A quantitative confocal study. *Hippocampus* **22**, 1242–1255 (2012).
63. W. Xu, T. C. Südhof, A neural circuit for memory specificity and generalization. *Science* **339**, 1290–1295 (2013).
64. D. C. Martinelli *et al.*, Expression of C1ql3 in discrete neuronal populations controls efferent synapse numbers and diverse behaviors. *Neuron* **91**, 1034–1051 (2016).